Lab on a Chip

Electronic Supplementary Information (ESI)

Extra figures, tables and videos

Table S1: Description of the parameters defined for COMSOL simulations to characterize the microfluidic system in terms of shear stress and lift forces applied to MDTs as well as oxygen and glucose uptake by the MDTs

Variable	Description	Value	References
Geometry			
T_{PDMS}	PDMS thickness (top and bottom)	3 mm	N/A
h_{well}	Well height	500 µm	N/A
w_{well}	Well width (square-bottom)	600 µm	N/A
$w_{channel}$	Channel width (square section)	600 µm	N/A
$L_{channel}$	Channel length	1 cm	N/A
$D_{interwell}$	Distance between wells	1.5 mm	N/A
d_{tissue}	Tissue diameter (381 ± 92 µm)	381 µm	N/A
Physical parameters			
ρ_{H2O}	Water density at 37°C	993.3 kg/m^3	Kestin, Sokolov & Wakeham[1]
η_{H2O}	Dynamic viscosity of water at 37°C	0.692 mPa s	Kestin, Sokolov & Wakeham[1]
ρ_{cell}	Density of cells in cancerous tissue	2.76 x 10^{14} cells/m^3	Experimental value (data not shown)
Diffusion parameters			
$D_{O2\text{-}PDMS}$	Diffusion of oxygen through PDMS	3.4 x 10^{-5} cm^2/s	Average from literature[2–4]
$D_{O2\text{-}H2O}$	Diffusion of oxygen through water	2.6 x 10^{-5} cm^2/s	Han & Bartels[5]
$D_{O2\text{-}tissue}$	Diffusion of oxygen through cancerous tissue	1.83 x 10^{-5} cm^2/s	Average from literature[6–10]
$D_{glucose\text{-}H2O}$	Diffusion of glucose through water	9.27 x 10^{-6} cm^2/s	Average from literature[2,6,11]
$D_{glucose\text{-}tissue}$	Diffusion of glucose through cancerous tissue	2.70 x 10^{-6} cm^2/s	Average from literature [6,9,12]
Solubility parameters			
$S_{O2\text{-}PDMS/H2O}$	Solubility of oxygen in PDMS *vs* H_2O	6.8	Average from literature [2,13]
$S_{O2\text{-}tissue/H2O}$	Solubility of oxygen in tissue *vs* H_2O	4.81	Average from literature [2,13]
$C_{glucose}$	Concentration of glucose in RPMI 1640 medium	11 x 10^{-3} mol/L	Wisent Bioproducts webpage[14]
C_{O2}	Concentration of oxygen in medium	0.2 x 10^{-3} mol/L	Henry's Law; Sander[15]
Michaelis-Menten uptake parameters			
$Q_{max\text{-}glucose}$	Maximum uptake rate of glucose by cancerous cells (cellular uptake)	0.39 x 10^{-16} mol/cell/s	Average from literature[6,9,16–18]
$Q_{max\text{-}O2}$	Maximum uptake rate of oxygen by cancerous cells (cellular uptake)	7.37 x 10^{-17} mol/cell/s	Average from literature[16,19,17,6,9]
$K_{glucose}$	Uptake saturation constant of glucose by cancerous cells	4.00 x 10^{-5} mol/L	Average from literature[6,9,11,16]
K_{O2}	Uptake saturation constant of oxygen by cancerous cells	4.63 x 10^{-6} mol/L	Average from literature[6,9,11,16]

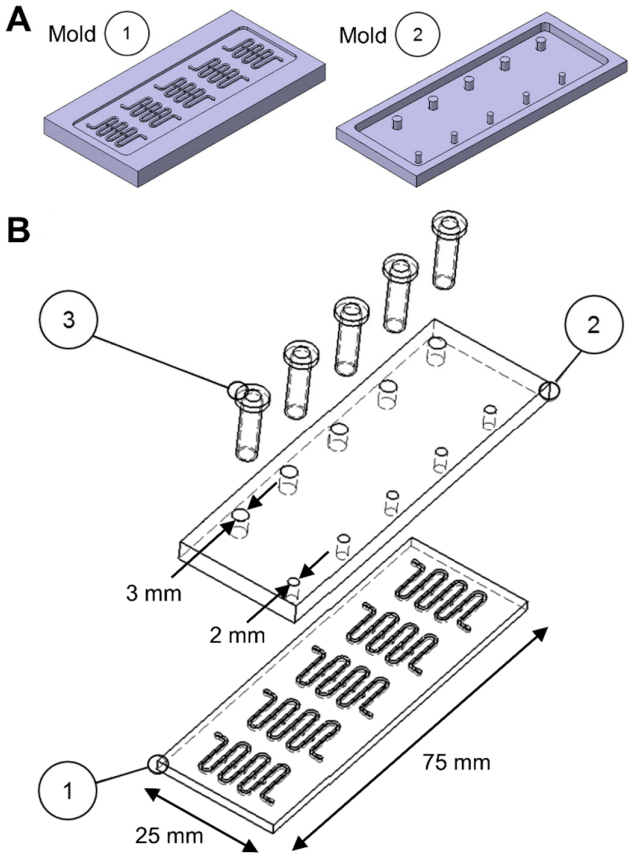

Fig. S1: Fabrication and assembly of the microfluidic platform. A) Mold 1 has features to form the channels and sedimentation traps of the bottom PDMS layer and mold 2 has cylindrical pillars to form the inlet and outlet holes in the top PDMS layer. B) Exploded view of the parts of the platform: 1- Bottom PDMS layer composed of channels and sedimentation traps, 2- top PDMS layer with five inlet holes and five outlet holes, and 3- five inlet reservoirs.

Table S2: Sedimentation velocities in infinite medium ($v_{sed,inf}$), approximation of tissue to loading medium differential density ($\Delta\rho$), and approximation of absolute densities (ρ) for different types of cancerous tissues

Type of tissue	$v_{sed,inf}$ (mm/s)	d (µm)	$\Delta\rho$ (kg/m^3)	ρ (kg/m^3)	n
22Rv1 MDTs (day 1)	1.92 ± 0.67	385 ± 31	21 ± 6	1027 ± 6	14
PC3 MDTs (day 1)	0.77 ± 0.18	350 ± 15	10 ± 2	1016 ± 2	5
MDTs OV90 (day 1)	2.08 ± 0.48	392 ± 26	22 ± 6	1028 ± 6	7
Average for MDTs	**1.59 ± 0.71**	**376 ± 22**	**18 ± 7**	**1024 ± 7**	
OV90 spheroids (day 7)	2.77 ± 0.30	412 ± 43	27 ± 6	1033 ± 6	20
TOV112D spheroids (day 7)	1.78 ± 0.54	366 ± 79	22 ± 6	1028 ± 6	29
Average for spheroids	**2.27 ± 0.70**	**389 ± 33**	**25 ± 4**	**1031 ± 4**	
Average for MDTs and spheroids	**1.86 ± 0.72**	**381 ± 24**	**21 ± 6**	**1027 ± 6**	

Each value is the mean for n measurements on independent samples ± standard deviation (s. d.). Average values ± s. d. for all three types of MDTs, for both types of spheroids, and for all five types of tissues are also shown.

Video S1: Demonstration of the platform loading procedure using fixed tissue samples. An air-displacement micropipette is used to induce a flow, thereby positioning the tissue sections above the sedimentation traps. Five MDTs (or spheroids) are typically loaded in less than one minute.

Details for the derivation of a critical diameter for non-vascularized tissue sections

The general equation describing a diffusive process where a component is being consumed is written as:

$$\frac{\partial C}{\partial t} = D\nabla^2 C - q. \quad (1)$$

In our case, we are looking at the constant consumption of oxygen by a spherical tissue sample located in infinite medium at steady-state. Two subdomains are defined: the tissue subdomain inside the tissue sample of finite size and the medium subdomain outside of this tissue sample.

Tissue subdomain

Within the tissue subdomain, it is supposed that oxygen is consumed by the cells at constant rate (q). Due to the spherical symmetry of the problem, the oxygen concentration (C) only varies along the direction of the radius (r). In steady state ($\partial C / \partial t = 0$) and after developing the Laplace operator in spherical coordinates, the equation thus simplifies to:

$$0 = D_T \frac{1}{r^2}\frac{\partial}{\partial r}\left(r^2 \frac{\partial C_T}{\partial r}\right) - q\,. \quad (2)$$

The concentration of oxygen inside the tissue (C_T) can be found by integrating this equation twice:

$$r^2 \frac{\partial C_T}{\partial r} = \frac{qr^3}{3D_T} + A\,, \quad (3)$$

$$C_T(r) = \frac{qr^2}{6D_T} - \frac{A}{r} + B\,, \quad (4)$$

where A and B are integration constants. Their expressions can be found using the boundary conditions of the problem. First, we are interested in finding a critical radius (R_c) for which oxygen only starts to be depleted at the center of the tissue in steady state ($C_T(r = 0) = 0$). Using this condition in equation (4) leads to $A = B = 0$. The second boundary condition serves to link both tissue subdomains together. An arbitrary concentration (C_0) is simply set at the surface of the tissue ($C_T(r = R_C) = C_0$), which leads to the following expression:

$$C_0 = \frac{q{R_C}^2}{6D_T}. \quad (5)$$

The oxygen concentration in the tissue subdomain ($r < R_C$) therefore follows the relationship:

$$C_T(r) = \frac{qr^2}{6D_T}. \quad (6)$$

Medium subdomain

In the medium subdomain outside the tissue, the consumption term (q) in equation (1) falls to zero due to the absence of cells consuming oxygen in this region. Once developed, the expression becomes:

$$0 = D_M \frac{1}{r^2}\frac{\partial}{\partial r}\left(r^2 \frac{\partial C_M}{\partial r}\right). \quad (7)$$

The concentration of oxygen in the medium (C_M) can be found once again by integrating two times:

$$\frac{\partial C_M}{\partial r} = \frac{E}{r^2}, \quad (8)$$

$$C_M(r) = F - \frac{E}{r}, \quad (9)$$

where E and F are integration constants, the expressions of which can be found using the boundary conditions outside the tissue. First, the concentration tends to the maximum dissolution concentration of oxygen in aqueous medium at 37°C (C_{max}) when r diverges to infinity ($C_M(r \to \infty) = C_{max}$), which leads to:

$$F = C_{max}. \quad (10)$$

Second, the continuity of the oxygen profile at the interface with the tissue requires that the concentration at the interface be equal to the same concentration (C_0) defined above ($C_M(r = R_C) = C_0$), which leads to:

$$E = R_C(C_{max} - C_0). \quad (11)$$

The oxygen concentration in the medium subdomain surrounding the tissue ($r > R_C$) is described by the following expression:

$$C_M(r) = C_{max} - \frac{R_C(C_{max} - C_0)}{r}. \quad (12)$$

Additional to the continuity of concentrations at the interface between the two subdomains, to respect mass conservation, the flux of molecules also needs to be equal:

$$-D_T \frac{\partial C_T}{\partial r}\Big|_{r=R_C} = -D_M \frac{\partial C_M}{\partial r}\Big|_{r=R_C}, \quad (13)$$

$$\frac{qR_C}{3} = \frac{D_M(C_{max} - C_0)}{R_C}. \quad (14)$$

Replacing C_0 with its expression in equation (5) yields:

$$\frac{qR_C}{3} = \frac{D_M\left(C_{max} - \frac{qR_C{}^2}{6D_T}\right)}{R_C}. \quad (15)$$

From this final equation, the critical diameter ($2R_C$) in non-perfused conditions is found:

$$2R_C = 2\sqrt{\frac{6D_T D_M C_{max}}{\rho Q(2D_T + D_M)}}. \quad (16)$$

Confocal microscopy image segmentation of live and dead cells

The image segmentation algorithm was developed to compute a semi-quantitative viability score from the fluorescent image sequences acquired by confocal microscopy. The chosen approach consists in segmenting the signal in both the green and red fluorescence channels, corresponding to signals from the live cells labelled with CellTracker Green (CTG) and dead cells labelled with propidium iodide (PI) respectively. Then, the relative area of the live signal over the total area of the live and dead signals is calculated. In order to better detect the lower intensity signal deeper in the sample, we used a modified version of Otsu's thresholding as described below (Fig. S2).

Description of the segmentation modules

Module 1: median filtering. Due to the rapid acquisition speed (400 lines/second) and the small number of photons detected in confocal microscopy, the image sequences are affected by shot noise. This first module is used to eliminate most of the noise present in the images without blurring the contours by applying a simple 3 x 3 median filter: the value of each pixel is reassigned to the median intensity value of the 9 surrounding pixels (including the pixel of interest)[20].

Module 2: signal equalization. Intensity variations were observed in our image sequences which were mainly due to the limited imaging depth in confocal microscopy and to inhomogeneous tissue staining that could not be corrected during acquisition. Therefore, this module aims to equalize the signal in both green and red channels so that all pixels to be segmented display similar intensity values. The image is simply multiplied by its inverted and blurred version obtained after applying a six pixel radius circular averaging filter.

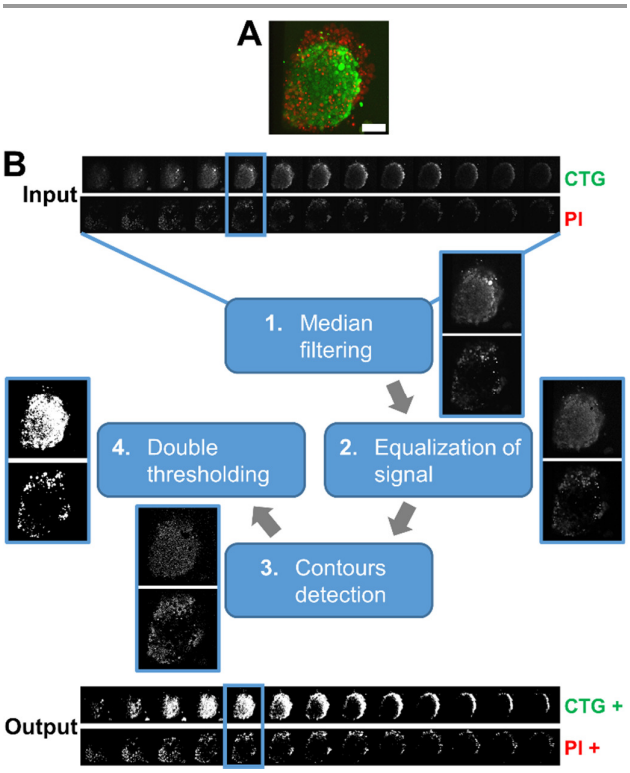

Fig. S2: Description of the image segmentation algorithm. A) Maximum projection of the image sequence used as an example to describe the modules of the algorithm (merged CTG and PI channels). B) Input image sequence showing the optical sections of the CTG and PI signals in separate channels, effect of each of the modules on the fifth set of optical sections, and resulting output segmented image sequence.

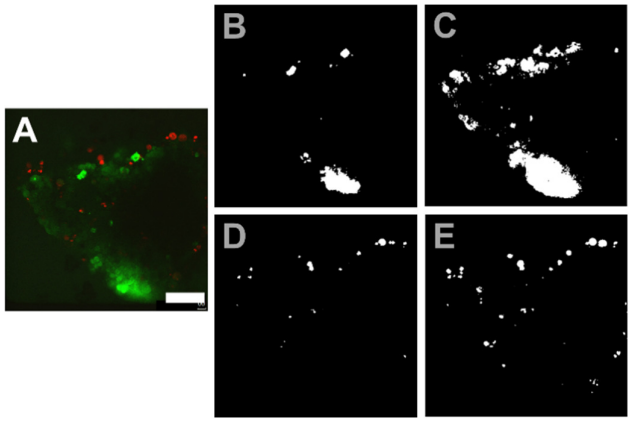

Fig. S3: Performance of the algorithm for low intensity signal. A) Optical slice (merged CTG and PI channels) of a MDT to be analysed. Scale bar = 100 µm. B-C) Result of the segmentation for the CTG (green) signal directly using Otsu's method on the filtered image (B) and using the modified algorithm (C). D-E) Result of the segmentation for the PI (red) signal directly using Otsu's method on the filtered image (D) and using the modified algorithm (E).

Module 3: detection of contours. A Laplacian filter is applied to the equalized image, and pixels with intensities above the 95th percentile are conserved. This measure of the second derivative of the image highlights regions on both sides of an edge with a steep intensity gradient[20].

Module 4: double thresholding. Segmentation of the green and red signals is finally accomplished by applying two thresholds. Since very high intensity pixels are lost while executing module 2, the first threshold is applied to the filtered image from module 1 and detects the saturated signal with an intensity above 75% of the saturation value (above 191 for an image with 256 levels of gray). The second threshold aims to detect positive signal of lower intensity. The equalized image from module 2 is used for thresholding using Otsu's method, but in order to reduce the contribution of the background signal, only the pixels associated to the contours detected in module 3 are considered. Otsu's method finds the threshold value that best separates the pixels into two classes by maximizing the inter-class variance[21]. The regions segmented by both thresholds are finally united.

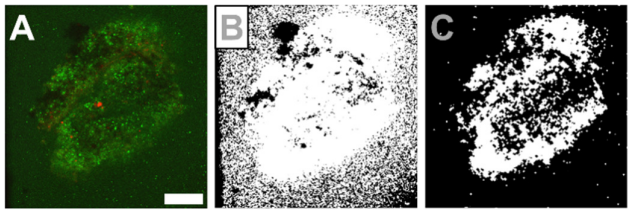

Fig. S4: Performance of the algorithm in the presence of background signal. A) Optical slice (merged CTG and PI channels) of a MDT to be analysed. Scale bar = 100 µm. B-C) Result of the segmentation for the CTG (green) signal directly using Otsu's method on the filtered image (B) and using the modified algorithm (C).

Post-segmentation calculations. From the segmented images, the viability score is simply calculated as the ratio of the area of the CTG signal over the total segmented area in both CTG and PI channels. In the case where segmented signals overlap at a specific pixel, a fraction of the unit area is attributed to each signal proportionally to the relative intensity of the associated pixels in the filtered image.

Performance of the algorithm

The algorithm segmented the images correctly in more than 95% of cases. The additional modules improve the detection of lower intensity positive signal (Fig. S3) and reduce the impact of background signal on segmentation efficiency (Fig. S4) compared to direct Otsu thresholding of the filtered image.

Details for the derivation of the inversely proportional scaling fit between time and volume (Fig. 3F)

The diffusion-reaction equation (1) describes the problem as a whole. In our case, because the channel is much longer than the MDT's size ($2R = d_{\text{tissue}} \ll L_{\text{channel}} = L$), we assume the system can be reduced to a symmetric 1D case of metabolite diffusion from the channel to the MDT (Fig. S5). This reduces equation (1) to the following:

$$\frac{\partial C(x,t)}{\partial t} = D_{\text{M}} \frac{\partial^2 C(x,t)}{\partial x^2} - q(x,t)\,, \tag{17}$$

where C and D_{M} are respectively the metabolite concentration in the system and diffusion constant in the medium. The metabolite uptake $q(x,t)$ is zero everywhere except in the MDT where it follows Michaelis-Menten kinetics.

$$q(x,t) = \begin{cases} q_{\max} \dfrac{C(x,t)}{C(x,t) + K_{\text{m}}} & x \le R \\ 0 & x > R \end{cases} \tag{18}$$

Two homogenous Neumann boundary conditions are necessary to consider both the symmetry at $x = 0$ and the absence of metabolite influx at $x = L/2$.

$$\left.\frac{\partial C}{\partial x}\right|_{x=0} = \left.\frac{\partial C}{\partial x}\right|_{x=L/2} = 0. \tag{19}$$

Extracting the MDT volume (V_{MDT}) requires a spatial integration over the entire volume with the system cross-section A and a multiplication by 2 due to symmetry to consider the actual 3D system. As $q(x,t)$ is non-zero only in the MDT, V_{MDT} appears by integrating this term.

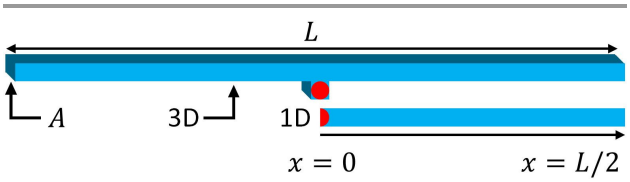

Fig. S5: Schematic of the 3D diffusion problem of cross-section A and length L reduced to a 1D diffusion problem of channel length $L/2$

$$2A\int_0^{\frac{L}{2}}\frac{\partial C}{\partial t}dx = 2AD_{\mathrm{M}}\int_0^{\frac{L}{2}}\frac{\partial^2 C}{\partial x^2}dx - 2A\int_0^{\frac{L}{2}}q(x,t)\,dx\,,$$
$$\frac{\partial n}{\partial t} = 2AD_{\mathrm{M}}\frac{\partial C}{\partial x}\Big|_{x=0}^{x=\frac{L}{2}} - 2A\int_0^{R}q(x,t)\,dx, \quad (20)$$

where n is the total number of moles of metabolite in the system. The first right-hand term is zero because of the homogenous Neumann boundary conditions. The second right-hand term gives the average value of $q(x,t)$ over the tissue volume $\bar{q}(t)$. Equation (20) thus becomes:

$$\frac{\partial n}{\partial t} = -\bar{q}(t)V_{\mathrm{MDT}}\,. \quad (21)$$

Considering that this problem must be solved for $C(x,t) \geq K_{\mathrm{m}}$, analyzing equation (18) shows that $q(x,t) \in [q_{\max}/2\,, q_{\max}]$. Therefore, we assume $\bar{q}(t)$ stays constant within that range over time and equation (21) can be solved:

$$n(t) - n(0) = -\bar{q}V_{\mathrm{MDT}}t\,. \quad (22)$$

The initial total number of moles of metabolite in the system is $n(0) = C_0V_{\mathrm{tot}}$ where C_0 is the initial metabolite concentration and V_{tot} is the total system volume. The following relation between time and volume can be derived:

$$t = \frac{C_0V_{\mathrm{tot}} - n(t)}{\bar{q}V_{\mathrm{MDT}}}. \quad (23)$$

Considering that $n(t)$ is such that the minimum concentration in the MDT is equal to K_{m}, for glucose and in the case of our simulations, we find that $n(0) \sim 20n(t) \gg n(t)$.

With this, we can write the following proportionality between time and volume:

$$t \propto \alpha\frac{C_0V_{\mathrm{tot}}}{\bar{q}}\frac{1}{V_{\mathrm{MDT}}} + \beta, \quad (24)$$

where α and β are proportionality constants that consider the complex geometry and time dependence of $\bar{q}$. In our case, $C_0V_0/\bar{q} \sim 0.71\ \mu\mathrm{L}\cdot\mathrm{h}$ which is on the same order as the fitted value of $1.11\ \mu\mathrm{L}\cdot\mathrm{h}$.

Details of the calculations of a carboplatin concentration for ovarian cancer patient MDTs

The recommended dosage for single-agent carboplatin in ovarian cancer patients is 360 mg/m^2.[22] Considering that women with ovarian cancer have an average body surface area of 1.71 m^2,[23] the recommended dose is 1.66 mmol of carboplatin. Assuming a blood volume of 4.7 L, we approximate that the maximum blood concentration of the drug in an average-sized woman would be about 350 μM.

References

1 J. Kestin, M. Sokolov and W. A. Wakeham, *J. Phys. Chem. Ref. Data*, 1978, **7**, 941.
2 K. Sumaru, S. Sugiura and T. Kanamori, *Biochem. Eng. J.*, 2007, **36**, 304–309.
3 D. A. Markov, E. M. Lillie, S. P. Garbett and L. J. McCawley, *Biomed. Microdevices*, 2014, **16**, 91–96.
4 M. E. Cox and B. Dunn, *J. Polym. Sci. Part A Polym. Chem.*, 1986, **24**, 621–636.
5 P. Han and D. M. Bartels, *J. Phys. Chem.*, 1996, **100**, 5597–5602.
6 A. Bertuzzi, A. Fasano, A. Gandolfi and C. Sinisgalli, *J. Theor. Biol.*, 2010, **262**, 142–150.
7 W. Mueller-Klieser, *Biophys. J.*, 1984, **46**, 343–348.
8 W. Mueller-Klieser, J. P. Freyer and R. M. Sutherland, *Br. J. Cancer*, 1986, **53**, 345–353.
9 R. Venkatasubramanian, M. A. Henson and N. S. Forbes, *J. Theor. Biol.*, 2008, **253**, 98–117.
10 J. Grote, R. Süsskind and P. Vaupel, *Pflügers Arch. Eur. J. Physiol.*, 1977, **372**, 37–42.
11 G. Hu and D. Li, *Biomed. Microdevices*, 2007, **9**, 315–23.
12 T. Kihara, J. Ito and J. Miyake, *PLoS One*, 2013, **8**.
13 M. C. Kim, R. H. W. Lam, T. Thorsen and H. H. Asada, *Microfluid. Nanofluidics*, 2013, **15**, 285–296.
14 Wisent Bioproducts, 2015.
15 R. Sander, *Atmos. Chem. Phys. Discuss.*, 2014, **14**, 29615–30521.
16 J. J. Casciari, S. V. Sotirchos and R. M. Sutherland, *J. Cell. Physiol.*, 1992, **151**, 386–394.
17 J. P. Freyer and R. M. Sutherland, *J. Cell. Physiol.*, 1985, **124**, 516–524.
18 D. C. Shrieve, D. F. Deen and J. W. Harris, *Cancer Res.*, 1983, **43**, 3521–3527.
19 C. J. Koch and J. E. Biaglow, *Br. J. Cancer. Suppl.*, 1978, **3**, 163–167.
20 R. C. Gonzalez and R. E. Woods, *Digital image processing*, Pearson Prentice Hall, Upper Saddle River, N.J., 3rd ed., 2008.
21 N. Otsu, *IEEE Trans. Syst. Man. Cybern.*, 1979, **9**, 62–66.
22 R. R. Barakat, M. Markman and M. Randall, *Principles and Practice of Gynecologic Oncology*, Wolters Kluwer, 5th ed., 2009.
23 J. J. Sacco, J. Botten, F. Macbeth, A. Bagust and P. Clark, *PLoS One*, 2010, **5**, 1–6.